Journal Pre-proof

Leading-Edge Separation Behaviors in SA RANS and SA-Based DDES: Simple Modifications for Improved Prediction

K. Kitamura , Y. Takagi , T. Harada , Y. Yasumura , M. Kanamori , A. Hashimoto

PII: S0045-7930(23)00039-7
DOI: https://doi.org/10.1016/j.compfluid.2023.105814
Reference: CAF 105814

To appear in: *Computers and Fluids*

Received date: 31 July 2020
Revised date: 22 December 2022
Accepted date: 2 February 2023

Highlights

- The SA-R RANS model coefficient C_rot = 2.0 is re-investigated.
- LES coefficient C_DES is calibrated for dissipation control in DDES (C_DES = 0.51).
- Dirty-cell (AR > 4) treatments in unstructured grids for smooth LES/RANS transition.
- As a result, a better leading-edge separation prediction is achieved for NASA CRM.

Leading-Edge Separation Behaviors in SA RANS and SA-Based DDES: Simple Modifications for Improved Prediction

K. Kitamura[a,*], Y. Takagi[a], T. Harada[a], Y. Yasumura[a], M. Kanamori[b], and A. Hashimoto[b]

[a]*Yokohama National University, Yokohama, Kanagawa 240-8501, Japan*

[b]*Japan Aerospace Exploration Agency (JAXA), Chofu, Tokyo 182-8522, Japan*

Abstract

[†]In this study, delayed detached-eddy simulations (DDESs) based on the Spalart–Allmaras turbulence model are investigated for separation flows. Three simple modifications are considered: the Reynolds-averaged Navier–Stokes (RANS) turbulence model coefficient, C_{rot}, is calibrated to achieve a better leading-edge separation prediction in DDES; the large-eddy simulation (LES) coefficient, C_{DES}, is assessed to obtain better dissipation control in DDES; and dirty-cell treatments in three-dimensional unstructured grids are conducted for a smooth LES/RANS transition. Numerical results confirm the effects of the three aforementioned steps, such as the reproducibility of the measured pressure distribution over the main wing in unsteady turbulence simulations of low-speed buffet around the NASA Common Research Model. Thus, these modifications will potentially serve as good alternatives, without major programming efforts, to the conventional approaches for practitioners.

Keywords: DDES, RANS, Spalart-Allmaras, HR-SLAU2, Buffet, Leading-Edge Separation

1. Introduction

Buffet phenomena are categorized as high-speed (associated with shock waves) at a transonic speed [1, 2] and low-speed at a subsonic speed [3], and both are of great engineering significance. Many aspects of flow physics are involved in the buffet phenomena. For example, Dandois et al. conducted a large-eddy simulation on the laminar

* corresponding author; tel: +81-45-339-3876, e-mail address: kitamura@ynu.ac.jp

† AR: aspect ratio; CFD: computational fluid dynamics; CRM: common research model; DDES: delayed detached-eddy simulations; JAXA: Japanese Aerospace Exploration Agency; LES: large-eddy simulation; RANS: Reynolds-averaged Navier–Stokes; SLAU: resolution simple low-dissipation advection upstream splitting method

transonic buffet, and revealed that its mechanism was different from a turbulent one [4]. Kouchi et al. experimentally investigated the effects of vortex generators on buffets using a fast-framing focusing Schlieren technique and wavelet analysis [5]. Nevertheless, numerical modeling of buffet phenomena is challenging. For example, to the best of our knowledge, for low-speed buffet simulations, no numerical solution currently available satisfactorily predicts the experimental data for the NASA Common Research Model (CRM) configuration [3]. In particular, it is extremely difficult to capture the leading-edge (L.E.) separation near the main wing root and its associated flow unsteadiness (presented in detail in Section 5).

Such unsteady, turbulent, and separated flow computations are computationally expensive. Thus, to achieve both efficiency and accuracy, hybrid methodologies are typically favored, such as delayed detached-eddy simulations (DDESs) [6], which combines Reynolds-averaged Navier–Stokes (RANS) modeling for boundary layers near the wall with large-eddy simulations (LES) elsewhere. However, it should be noted that DDES involves many parameters (e.g., the LES coefficient C_{DES}, which controls LES/RANS transitions [7]) that must be appropriately adjusted by users. In addition, the DDES performance is highly dependent on the selected RANS models, such as Spalart–Allmaras (SA)-type models. These models include original SA [8], SA-noft2 [9], SA with rotation correction (SA-R) [10, 11]), SA-noft2-R (with RANS turbulence model coefficient C_{rot} = 1.0 [12], and C_{rot} = 2.0 [13]), SA with rotation and curvature correction (SA-RC) [14]. NASA's turbulence modeling resource [13] details the models and classifications.

As aforementioned, a leading-edge separation occurs in the low-speed buffet, and the separation point belongs to the RANS part, as shown in Fig. 1. For those separated flows, the behaviors of RANS modeling still have a room for discussions on potential improvements of its separation predictability. For example, the SA-R model by Dacles-Mariani et al. [10, 11] was designed to "suppress turbulence viscosity," where pure rotation is considered to exceed both the strain rate and turbulence effects, such as in a vortex core. This concept sounds reasonable; however, the modification of the value of C_{rot} was essentially arbitrary. In addition, *when it is coupled with LES as a part of DDES* [6, 15, 16], *the behavior of such a modified RANS model remains unknown* [17]. As reviewed by Spalart [18], the first version DES [15] (denoted as "DES97") achieved certain success in hybridizing RANS and LES in a simple and economical manner but suffered from grid-induced flow separation. DDES [6] resolved this problem by introducing the f_d function, which tends to zero toward the wall. Improved DDES (IDDES) further modified DDES but with additional complexity [16]. This may partially explain why DDES remains popular, and other modifications have been proposed on DDES. For instance, the grid sensitivity of DDES was reported by Spalart et al. [19].

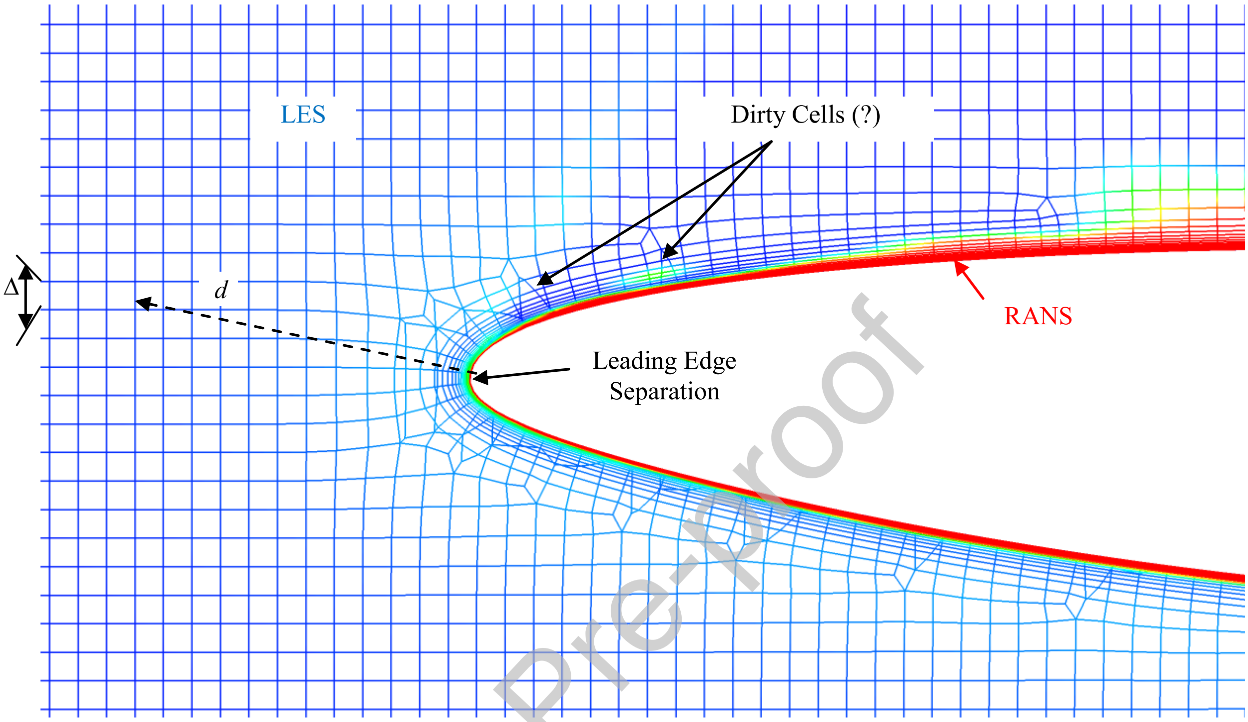

Fig. 1. Computational grid near the leading-edge of NASA CRM main wing, colored with (non-dimensional length scale) = (LES length scale Δ) / (RANS length scale *d*). 0 (blue) almost corresponds to LES regions, and 1 (red) for RANS regions (In actuality, the function f_d leads all of the near-wall regions to RANS).

The present study offers simple modifications to DDES suitable for a low-speed buffet involving a leading-edge separation. Special focus is given to C_{rot}, which is the modification parameter from SA to SA-R (details provided in Section 3.1., and tested in subsonic and even supersonic cases in sections 4.1 and 4.2., respectively, in contrast with literature [10, 11]), and C_{DES}, which is a transition parameter between RANS and LES, is calibrated for a practical buffet case, in contrast to the isotropic turbulence case in [7]. Furthermore, the numerical flux function is revisited.

Recent efforts on unsteady separated flows (represented by the buffet) include the Stanford University Unstructured (SU2) code [20], in which the high-resolution simple low-dissipation advection upstream splitting method 2 (HR-SLAU2) [21] numerical flux is employed for IDDES. The HR-SLAU2 is a successor of SLAU2 [22] (an 'all-speed' flux capable of accurately computing both low and high Mach flows, similarly to [23]), having a reduced dissipation term in its pressure flux for smooth flows, and was inspired by a low-dissipation version of the Roe flux (HR-Roe) [7,24,25]. Mohamed et al. [7] proposed a reduction of C_{DES} from 0.65 to 0.51 for such a low-dissipation flux function. However, in [21], HR-SLAU2 was not investigated in its complete form, having the f_d function borrowed from DDES, in contrast with HR-Roe (proposed by Mohamed et al. [7]) because it was tested in inviscid or laminar flows only. Therefore, this work is the first attempt to restore the f_d function in HR-SLAU2 for DDES while controlling C_{DES}.

Furthermore, as in other practical simulations, we used three-dimensional (3D) unstructured grids that were generated by HexaGrid [26] or MEGG3D [27] and a 3D unstructured grid solver "FaSTAR," [28], which were all developed by the Japanese Aerospace Exploration Agency (JAXA). The HexaGrid generates Cartesian-based grids (mostly consisting of cubes); however, as with other meshing tools, it also produces cells whose aspect ratio (*A*R) significantly deviates from unity [29]. As such, the length scale and subsequent RANS/LES transition may be erroneous for these cells unless it is carefully modified, as in the present work. MEGG3D generates tetrahedra cells away from the body and prism cells near the wall, which also raises concerns of sudden cell-size jumps at their conjunctions. This software is suitable for retaining the original body configurations of small devices, such as fins.

This study revisits DDES with simple modifications for various aerodynamic analyses, such as a low-speed buffet, in which i) the SA-R coefficient, C_{rot}, is re-investigated for a better leading-edge separation prediction in DDES, ii) the LES/RANS boundary (C_{DES}) is calibrated for dissipation control in DDES, and iii) dirty-cell treatments are performed in 3D unstructured grids for a smooth LES/RANS transition. We expect that the present modifications will be used by practitioners in many simulations of engineering importance such as in [5, 30].

2. Governing Equations

The governing equations are 3D compressible Navier–Stokes equations expressed in the RANS form as follows (1, 2, and 3 are substituted for the subscripts *k*, *l*, *m*, and *n*).

$$\frac{\partial \mathbf{Q}}{\partial t} + \frac{\partial \mathbf{F}_k}{\partial x_k} = \frac{\partial \mathbf{Fv}_k}{\partial x_k} \tag{1a}$$

$$\mathbf{Q} = \begin{bmatrix} \rho \\ \rho u_l \\ \rho E \end{bmatrix}, \quad \mathbf{F}_k = \begin{bmatrix} \rho u_k \\ \rho u_l u_k + p\delta_{lk} \\ \rho u_k H \end{bmatrix}, \quad \mathbf{Fv}_k = \begin{bmatrix} 0 \\ \tau_{lk} \\ u_m \tau_{mk} + (\kappa + \kappa_t)\dfrac{\partial T}{\partial x_k} \end{bmatrix} \tag{1b}$$

$$\tau_{lk} = (\mu + \mu_t)\left[\left(\frac{\partial u_l}{\partial x_k} + \frac{\partial u_k}{\partial x_l}\right) - \frac{2}{3}\frac{\partial u_n}{\partial x_n}\delta_{lk}\right] \tag{1c}$$

where ρ is the density, u_k is the velocity of the components in Cartesian coordinates (k = 1, 2, 3 correspond to u, v, w, respectively), E is the total energy per unit mass, p is the pressure, H is the total enthalpy ($H = E + (p/\rho)$), and T is the temperature. The working gas is air, which is approximated by the calorically perfect gas model with the specific heat ratio γ =1.4. The Prandtl number Pr = 0.71. The molecular viscosity, μ, which is calculated using Sutherland's formula [31] and the thermal conductivity, κ, is related by the formula $\kappa = c_p\mu/\mathrm{Pr}$, where c_p is the specific heat at constant pressure. In the turbulence calculations, the molecular viscosity, μ, is replaced by ($\mu+\mu_t$), where μ_t is the turbulence viscosity; similarly, κ is replaced by ($\kappa + c_p\mu_t/\mathrm{Pr}_t$), and Pr_t is the turbulent Prandtl number, 0.90.

Eq. (1) is discretized using the finite-volume method as follows:

$$\frac{V_i}{\Delta t}\Delta \mathbf{Q}_i + \sum_j (\mathbf{F}_{i,j} - \mathbf{Fv}_{i,j})S_{i,j} = 0 \tag{2}$$

where V_i stands for the volume of the cell i, Δt is the time step, $\Delta \mathbf{Q}_i$ is the change of conservative variables in time, and $\mathbf{F}_{i,j}$ and $\mathbf{Fv}_{i,j}$ are the inviscid (Euler) and viscous fluxes through the cell-interface $S_{i,j}$ (which separates the cell i and its neighbor cell j), respectively (see Fig. 2 for a cell geometric schematic).

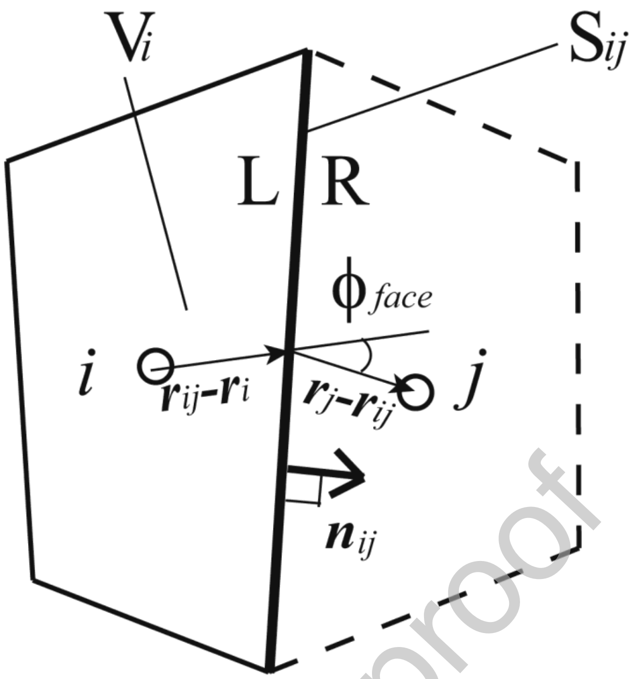

Fig. 2. Schematic of cell geometries.

3. Numerical Methods: DDES and Proposed Modifications

3.1. C_{rot} in SA-noft2-R model

Improvements to the SA model, such as SA-R and SA-RC, have been proposed to control excess leading-edge separations. These modifications were intended to remedy the weakness of the SA (SA cannot distinguish the turbulent vorticity from the pure vorticity, which is high for a flow around a body-wall with curvature [10, 11]). These corrections are effective but require a user-specified parameter, which significantly alters the solution. For instance, in SA-R [10, 11] the vorticity magnitude $|\omega|$ is replaced as follows.

$$|\omega| \to |\omega| + C_{rot}\min\left(0, |s| - |\omega|\right) \tag{3}$$

where $|s|$ is the strain-rate

$$|s| = \sqrt{2S_{ij}S_{ij}}, S_{ij} = \frac{1}{2}\left(\frac{\partial u_i}{\partial x_j} + \frac{\partial u_j}{\partial x_i}\right) \tag{4}$$

Note that there is room for arguments on the value C_{rot}. Dacles-Mariani et al. [10, 11] initially proposed this modification on the Baldwin–Barth model [32] rather than the SA model. Furthermore, the value of C_{rot} was adopted arbitrarily. NASA's turbulence model resource [13] recommends $C_{rot} = 2.0$, while Lei [12] claims that $C_{rot} = 1.0$ is the best, as "$C_{rot} = 2.0$ is physically incorrect." The value of $C_{rot} = 1.0$ appears to be widely used, at least in Japan [28]. In addition, the model coefficients in the SA-RC model are also debated in a similar manner [14].

Furthermore, such discussions apply only to its use as a RANS model, and not for DDES, which is its combined form with LES. Therefore, in this study, we investigate the effects of C_{rot} in case of both RANS and DDES. For the RANS model, we employ the "SA-noft2" model (in which the tripping term is absent [9]) or its modified form "SA-noft2-R" for separated flows (see Appendix for details), rather than the original SA model.

3.2. C_{DES} in (SA-noft2-R-based) DDES

C_{DES}, which controls the LES/RANS transition, is briefly reviewed in this subsection. First, the length scale in DDES is given as

$$\tilde{d} = d - f_d \max(0, d - C_{DES}\Delta) \tag{5}$$

where d is the distance from the wall (Fig. 1), which is the length scale of the SA RANS model (see Appendix for more details). Δ is the length scale of LES, which corresponds to the edge length for the cube. C_{DES} is typically set at 0.65 [33], and if it is large, $\tilde{d}$ approaches d and the RANS region extends. On the contrary, the smaller the value of C_{DES}, the closer $\tilde{d}$ tends to be to Δ, leading to the larger LES zone. In this study, following Mohamed et al. [7], we attempt to decrease C_{DES} and broaden the LES region.

In addition, the f_d function is given as

$$f_d = 1 - \tanh\left(8^3 r_d^3\right) \tag{6}$$

$$r_d = \frac{\tilde{\nu}}{\sqrt{u_{i,j}u_{i,j}}\,\kappa^2 d^2} \tag{7}$$

so it approaches unity in the LES region and 0 within the attached boundary-layers [8], where $\tilde{\nu}$ is a working variable in the SA model, and κ is the Karman constant.

3.3. HR-SLAU2 for DDES

The numerical flux function, HR-SLAU2, was proposed and tested in one-dimensional (1D), two-dimensional (2D), and 3D meshes that were smoothly structured [21]. Here, it is extended to DDES on unstructured 3D meshes of general quality, which contain dirty-cells. The dirty-cells are

i) "A face is composed of nodes (four or more) that are not on the same plane" (Fig. 3a)

ii) "A (hexahedral or prism) cell is composed of its upper face and lower face, which are partly flipped over in their relative positioning" (Fig. 3b)

iii) "A cell is composed of edges intersecting faces" (Fig. 3c). In such cells, the cell volume can be "very small, or even negative, leading to divergence of flow computations" [29].

Additional discussions on this topic will be provided in Section 3.4.

a) **b)** **c)**

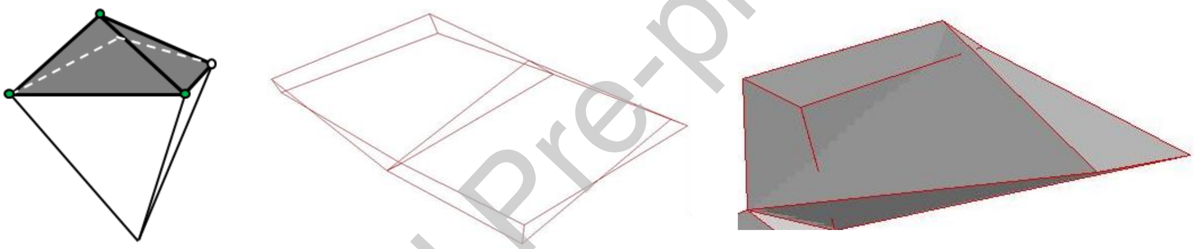

Fig. 3. Dirty-cell examples (a) (gray) face composed of four points not on the same plane, (b) upper and lower surfaces flip-over and (c) edge-face interaction.[28)]

HR-SLAU2 and HR-Roe were inherently designed to have reduced dissipation [25] at the LES region, and Mohamed et al. [7] introduced the f_d function from DDES to distinguish between the RANS and LES zones.

The HR-Roe is written as follows:

$$\mathbf{F}_{HR-Roe} = \frac{1}{2}(\mathbf{F}_L + \mathbf{F}_R) - \frac{\gamma_{HR}}{2}|\hat{\mathbf{A}}| \cdot (\mathbf{Q}_R - \mathbf{Q}_L) \quad (8)$$

where the first term on the right-hand-side, $\frac{1}{2}(\mathbf{F}_L + \mathbf{F}_R)$, is a central-difference term, and the second term, $-\frac{\gamma_{HR}}{2}|\hat{\mathbf{A}}| \cdot (\mathbf{Q}_R - \mathbf{Q}_L)$, corresponds to the numerical dissipation. Similarly, in HR-SLAU2, as detailed in [21], the pressure flux is modified (from SLAU2) as

$$(\tilde{p})_{HR-SLAU2} = \frac{p_L + p_R}{2} + \frac{\mathrm{P}^+\big|_{\alpha=0} - \mathrm{P}^-\big|_{\alpha=0}}{2}(p_L - p_R) + \gamma_{HR} \cdot \sqrt{\frac{\mathbf{u}_L{}^2 + \mathbf{u}_R{}^2}{2}} \cdot \left(\mathrm{P}^+\big|_{\alpha=0} + \mathrm{P}^-\big|_{\alpha=0} - 1\right)\overline{\rho c} \tag{9}$$

where γ_{HR} is between 0 and 1 (γ_{HR} = 0 reduces HR-Roe to the central-difference, and if γ_{HR} = 1, the original Roe or SLAU2 is recovered). However, the actual setting of γ_{HR} = 0 reportedly destabilized the computation, and thus it was set by Winkler et al. [25] as

$$\gamma_{HR} = \max(\gamma_{\min}, \quad \gamma_2, \quad \gamma_w) \tag{10}$$

where $\gamma_{\min}$ = 0.2 according to [21]. The details are found in [21], but this $\gamma_{\min}$ detects spatial oscillations.

Here, γ_2 is given as

$$\gamma_2 = \begin{cases} 1 & \phi_{face} \ge 120^\circ \\ 1 - f_d \cdot \left[\frac{2}{3}\cos(\phi_{face}) + \frac{1}{3}\right] & 0^\circ \le \phi_{face} < 120^\circ \end{cases} \tag{11}$$

where ϕ_{face} is an angle created by the *i*-th cell center, *j*-th cell center, and their interfacial center *ij* (Fig. 2). If these three points are aligned in one straight line, the angle is zero, and γ_2 = 0 (when f_d = 1). If ϕ_{face} exceeds 120°, the original Roe or SLAU2 is recovered. Now, f_d is a function that is borrowed from DDES [6], which was simply assumed as unity for inviscid or laminar flows when HR-SLAU2 was first proposed and examined [21].

In this work, this f_d function is activated in HR-SLAU2, and its inherent ability is turned on to distinguish LES and RANS regions.

3.4. Dirty-Cell Treatments for Better LES/RANS Transitions

Typical automatically generated cells are of poor quality at the conjunction between the mesh around the body (prisms for HexaGrid) and the mesh away from the body (cubes for HexaGrid). These dirty cells (highlighted in Figs. 1 and 3) have less accurate volumes, and can therefore be categorized into a RANS zone even though they may be surrounded by LES cells. In order to prevent this, we propose the following modification.

$$\Delta \to \min\left(1, \frac{4}{AR}\right) \cdot \Delta \tag{12}$$

where AR is the cell Aspect-Ratio [29] defined as follows (see Fig. 2 for V_i and S_{ij}).

$$AR \cong \max\left(\frac{V_i^{2/3}}{S_{i,j}}, \quad \frac{V_j^{2/3}}{S_{i,j}}, \quad \frac{S_{i,j}}{V_i^{2/3}}, \quad \frac{S_{i,j}}{V_j^{2/3}} \right) \tag{13}$$

This modification was explained in [29] as: "i) the cell length normal to the interface is approximated by $b \equiv V_{i\ or\ j}/S_{i,j}$, where $V_{i\ or\ j}$ is the cell volume and $S_{i,j}$ is the interface area; ii) the cell length tangential to the interface, on the other hand, is represented by $a \equiv V_i^{1/3}$; iii) then, $AR \equiv b/a$, and its inverse are obtained for both i and j cells; iv) finally, its maximum value is adopted for evaluation". This modification proposed in [29] is expected to work at dirty-cells and to effectively suppress the erroneous Δ values, based on the following facts [29].

- The AR value of the cube is unity, and exceeds this value near the wall or where the cell sizes change abruptly.
- The Eq. (13) needs only little additional information because the cell volumes V_i, V_j and the interfacial area $S_{i,j}$ used here are necessary components of the solver, as seen in Eq. (2). Thus, these are already known or readily available on an unstructured grid solver.

4. RANS Numerical Examples for C_{rot}

In this section, we investigate the C_{rot} value of the SA-noft2-R model in two selected RANS examples. Note that these examples are not closely related from shock-related instabilities of point-nosed slender bodies [34], in which the instabilities propagate upstream within the (subsonic) boundary layer and then change the upstream shock configurations.

4.1. Low-Speed Flow around Slender Body with Fins

The first example is a low-speed flow around a slender body equipped with fins (Fig. 4). This configuration can be suitable for a reusable rocket. It consists of a sphere-nose, cone-forebody, and a square-cylindered aft body (the cone is smoothly connected to the square-cylinder). The details for this configuration and its aerodynamics are found in previous studies [35, 36].

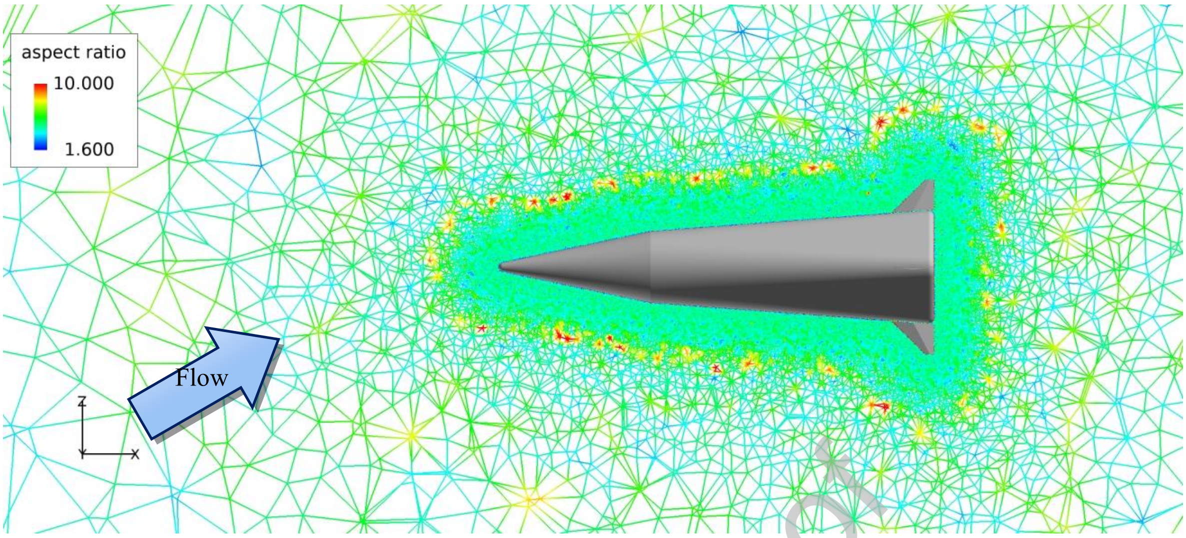

Fig. 4. Computational mesh around finned-slender-body (The computational domain is a cube of 30L × 30L × 30L).

As the reference Mach number was low (M = 0.086), the preconditioned LU-SGS [37] (for time integration) was used along with the all-speed numerical flux SLAU. The Green–Gauss method was used for the slope computation along with Venkatakrishnan [38] limiter. U-MUSCL scheme [39] (third-order at maximum in space) was employed for reconstruction. The Reynolds number based on the body length L was 6×10^5, and the SA-noft2-R model (C_{rot}= 0.0, 1.0, or 2.0) was used to compute the turbulent viscosity. The angle-of-attack, α, is 30°, which produces a massive flow separation.

The computational grid was generated by using MEGG3D [27]. The region away from the body surface was discretized with tetrahedral cells (in contrast with cubes generated by HexaGrid) whereas the region around the body was constructed with prism layers with the first cells nearest to the wall with a height of $O(-3)$ L height ($y^+ < 1$, maximum $AR \approx 150$), and the total number of cells was approximately 35 million (Fig. 4); the grid convergence was confirmed in [36] with C_{rot}= 1.0. A delta wing with a 60° sweep angle was employed as the fin, which had an area corresponding to approximately 10% of that of the body base. An experimental value of the pitching moment coefficient (approximately 65% of the body length from the nose), $C_m = 0.068$ [36], was used. We will compare our computed solutions obtained using this value to examine the effect of C_{rot}. The model configuration is detailed in [36].

The results are shown in Figs. 5–7. A C_{rot} value of 2.0 resulted in the best match (0.057) with the experiment (0.068) (Fig. 5). In the case where C_{rot} = 2.0, the magnitude of the negative moment generated by the fins (“Fin”) was relatively small, which cancelled out a portion of the positive moment created by the main body (“Body”), and thus, the total (positive) C_m ("Total") remained large. This will be further discussed based on visualized solutions.

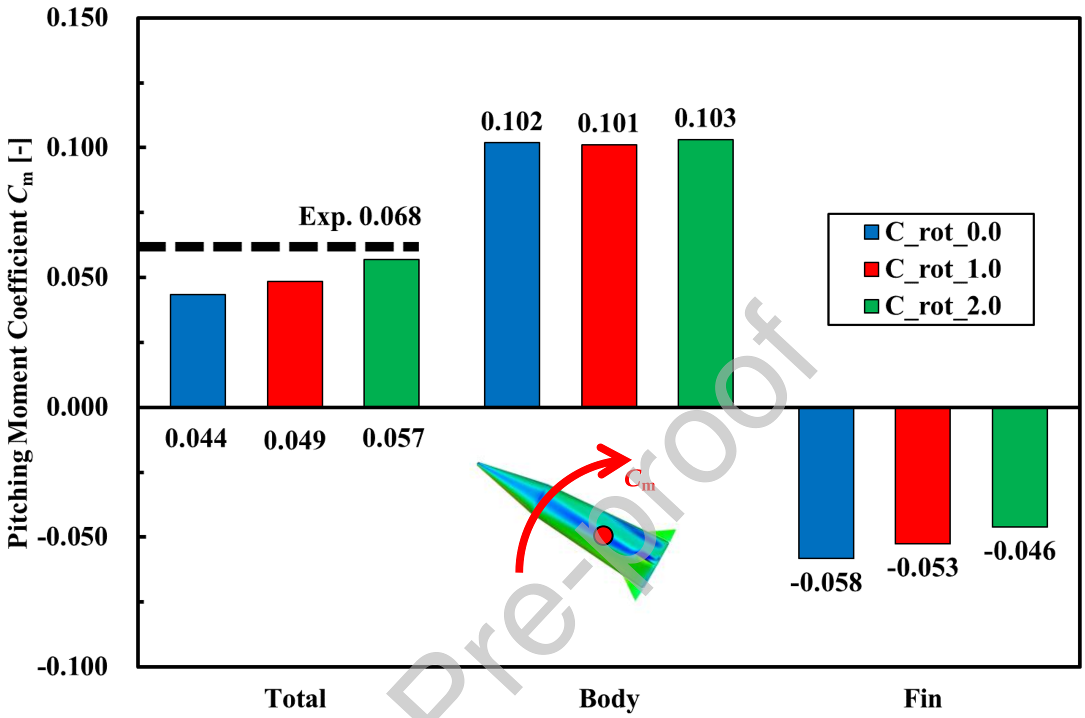

Fig. 5. Computational results for low-speed flow around finned-slender-body: Pitching moment C_m.

According to Fig. 6, a pair of vortices, V1 from the body nose and V2 from the body side, coalesced (as "V1+V2") at the rear portion of the body in the cases where C_{rot} = 1.0 and 2.0, whereas they independently existed in the case where C_{rot} = 0.0. This is considered as pure rotation effects, where the turbulent effects were treated separately in the cases with C_{rot} = 1.0 and 2.0, which prevented excess amounts of turbulent viscosity from leaving V1 and V2 undiffused at the downstream, as opposed to the case with C_{rot} = 0.0, in which these vorticities were totally regarded as turbulent.

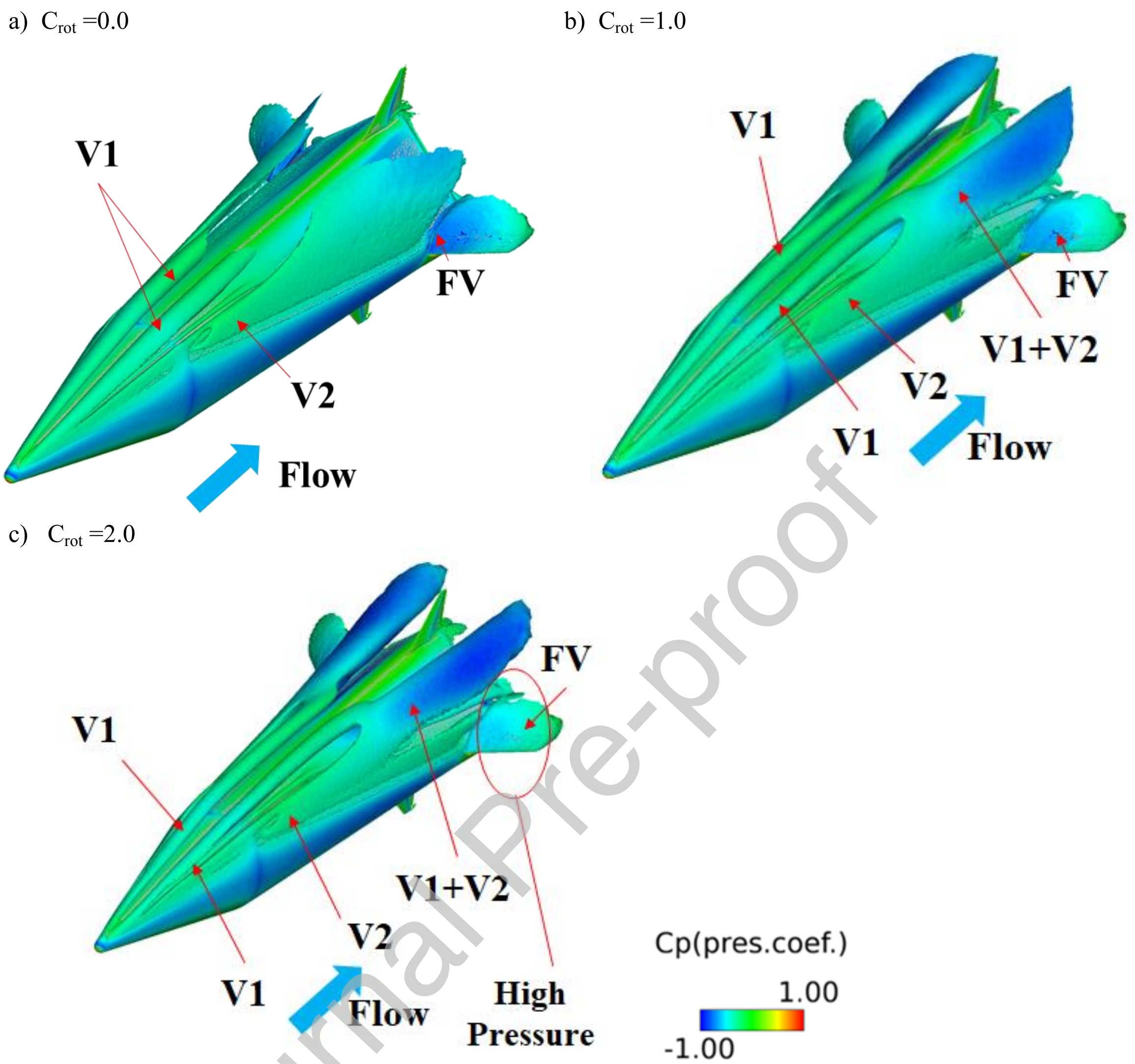

Fig. 6. Computational results for low-speed flow around finned-slender-body: iso-surfaces of Q, colored with $-1<C_p<1$, (a) C_{rot} = 0.0, (b) C_{rot} = 1.0, (c) C_{rot} = 2.0.

With regard to the vortices FV (fin vortices) created at the fins, they clearly lowered the pressure over the fins for the cases where C_{rot} = 0.0 and 1.0, but hardly did so in the case where C_{rot} = 2.0 (red circle in Fig. 6c). This is considered to have suppressed the negative pitching moment by the fins when C_{rot} = 2.0 (Fig. 5). This will be further discussed using Fig. 7, which presents the pressure distributions at the η = 74.5% cross-section (as indicated by a red line in Fig. 7a) over the fin surface (Fig. 7b) and its surrounding flow fields (Figs. 7c-e).

From Fig. 7b, it can be seen that the surface pressure distributions are actually different among the different C_{rot} cases. In particular, the magnitude and the extent of the separation over the upper surface tend to decrease with an increase of C_{rot}, i.e., C_{rot} = 0.0, 1.0, and 2.0. This separation zone creates a negative pressure (i.e., the pressure over the fin is low) (Fig. 7b), as shown in Fig. 6. Consequently, the negative moment created by the fins was small when C_{rot} = 2.0, and therefore, the total pitching moment was eventually the closest to the reference value (Fig. 5). This is presumably because:

- C_{rot} = 2.0: Only the turbulent effects were taken into account in the RANS model, and the flow separation still occurred.
- C_{rot} = 0.0: The separation occurred owing to both the turbulent and pure rotation effects.
- C_{rot} = 1.0: In the middle of these two.

Therefore, as opposed to the V1+V2 formation, the FV around the fins was suppressed for a large C_{rot}. This difference resulted from the following scenario: i) The turbulent boundary layer sufficiently developed and then separated from the wall downstream from the previous case, and around the main body in the present case; ii) However, the fins here were exposed to a uniform flow, and thus, the boundary layer may have been separated before or during its development. In most of the leading-edge separation cases, the boundary layer would have separated before its development.

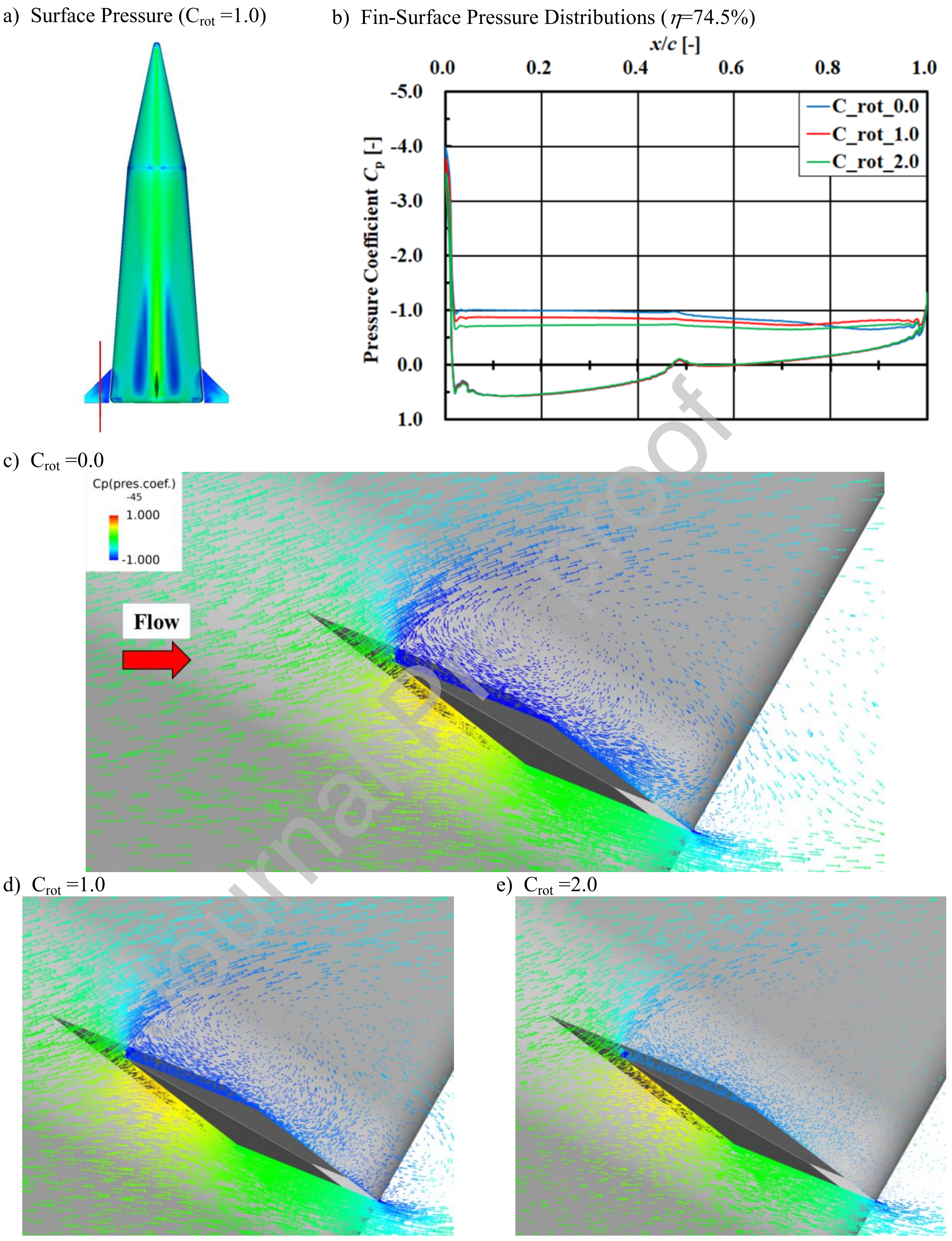

Fig. 7. Computational results obtained for low-speed flow around finned-slender-body: (a) Surface pressure distributions along with η=74.5% cross-section (red line) (C_{rot} =1.0), (b) Pressure distribution at η=74.5% cross-section, (c) Velocity vectors around the fin at the η=74.5% cross-section, colored with $-1<C_p<1$ (C_{rot} =0.0), (d) (C_{rot} = 1.0), and (e) (C_{rot} = 2.0).

4.2. Supersonic Flow around Slender Body

The second example is a Mach 1.5, Re = 1.38×10^7 supersonic flow around a slender body. The angle of attack is 15°, and it was confirmed that steady RANS solutions sufficiently agreed with the experiment up to this angle [40, 41]. The computational grid is composed of 44 million cells, whose grid convergence was confirmed previously [38, 39]. The grid topology shown in Fig. 8 (covering 20L × 20L × 20L cube filled with hexahedra, prisms, pyramids, and tetrahedra; generated by HexaGrid; maximum $AR \approx 90$ closest to the body; $y^+ < 1$) features an axisymmetric slender body with a protuberance (6% of the body length L, and its height is 15% the body diameter D) located at 22% downstream from the nose and 45° from the upper surface (centerplane), only on the port side. This arrangement induces prominent flow asymmetry.

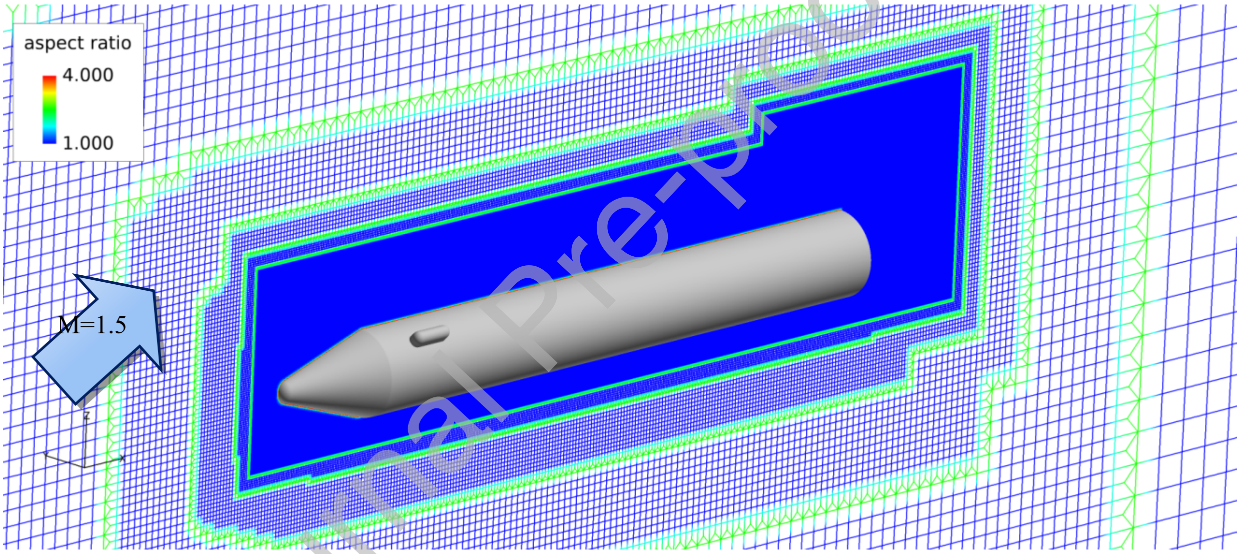

Fig. 8. Computational mesh around slender body. The computational domain is a cube of 20L × 20L × 20L.

The computational methods employed here are listed as follows: Green-Gauss [42] for gradient evaluations with the minmod slope limiter [43]; MUSCL [44] (second-order in space) for the reconstruction of physical variables using the slope to obtain cell-interfacial values; SLAU [45] numerical flux function; and LU-SGS [46] for time evolution. The turbulent viscosity, μ_t, was computed using the SA-noft2-R model (C_{rot} = 0.0, 1.0, or 2.0; C_{rot} = 0.0 corresponds to the original SA-noft2 model; C_{rot} = 1.0 corresponds to Refs. [40, 41]).

The computed solutions are visualized in Fig. 9 (vorticity) and Fig. 10 (turbulent viscosity). It is observed that the solutions changed according to the choice of C_{rot}.

- As C_{rot} increased, the vorticity grew but the turbulent viscosity reduced at the port side in the downstream portion. In other words, for a large C_{rot}, the downstream vorticity was considered to have resulted from a pure rotation, instead of turbulence. This corresponds to the design concept of the SA-R model.
- For C_{rot} = 0.0, the vortex in the port side was elongated in the longitudinal direction. However, for C_{rot} = 1.0 and 2.0, the vortices had almost the same shape, albeit with different vorticity and turbulent viscosity values.

a) C_{rot} =0.0 b) C_{rot} =1.0 c) C_{rot} =2.0

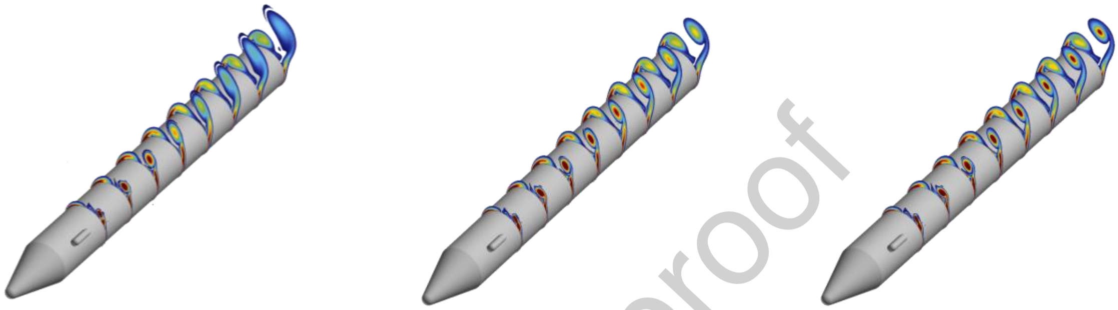

Fig. 9. Simulated supersonic flow around slender body: x-directional vorticity magnitude distributions, $0<|\omega_x|<0.2$ (a) C_{rot} =0.0, (b) C_{rot} =1.0, (c) C_{rot} =2.0.

a) C_{rot} =0.0 b) C_{rot} =1.0 c) C_{rot} =2.0

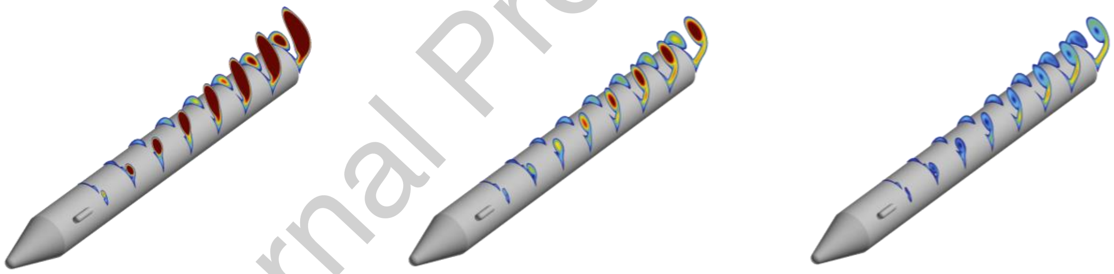

Fig. 10. Simulated supersonic flow around slender body: turbulent viscosity distributions, $0<\mu_t/\mu<1000$, (a) C_{rot} =0.0, (b) C_{rot} =1.0, (c) C_{rot} =2.0.

Then, the obtained aerodynamic coefficients are compared, where C_A is an axial force coefficient and C_Y is a lateral force coefficient. The comparison can be seen in Table 1. While deriving the axial force coefficient C_A, the base pressure was corrected as there was a sting mounted behind the experimental model. Pressure values at four pressure sensors around the sting on the base were averaged, and the resultant base pressure was used to account for the sting effects.

Table 1. Supersonic aerodynamic characteristics of slender body.

	C_A	C_Y
C_{rot} =0.0	0.780	0.829
C_{rot} =1.0 [38]	0.772	0.849
C_{rot} =2.0	0.764	0.850
Experiment [39]	0.756±0.126	0.822±0.078

According to Table 1, the computed C_A approached the (averaged) experimental value as C_{rot} increased and C_Y deviated (however, the values were within the error margins). Although it is difficult to determine which was more efficient between C_{rot} = 1.0 and 2.0 based on the results, it can be said that both of the cases performed as designed, when compared with C_{rot} = 0.0.

5. 3D Low-Speed Buffet Flow Computation

In this section, we present the computations of the 3D, unsteady, low-speed buffet flow around the aircraft with Mach 0.25, Re = 1.16×10^7 and an angle of attack of 18° [3]. The body configuration and the corresponding computational mesh (having approximately 23 million cells) are shown in Fig. 11a; this figure is colored based on the *AR*. The *AR* value is higher at the junctions of different cell sizes, including many dirty cells (Fig. 3) or near the wall, while it is unity elsewhere (i.e., cubes). In this DDES case, a grid convergence study was not conducted since refining or coarsening the grid density will *automatically* shift the RANS/LES transition location, which is not our intension.

a) Grid

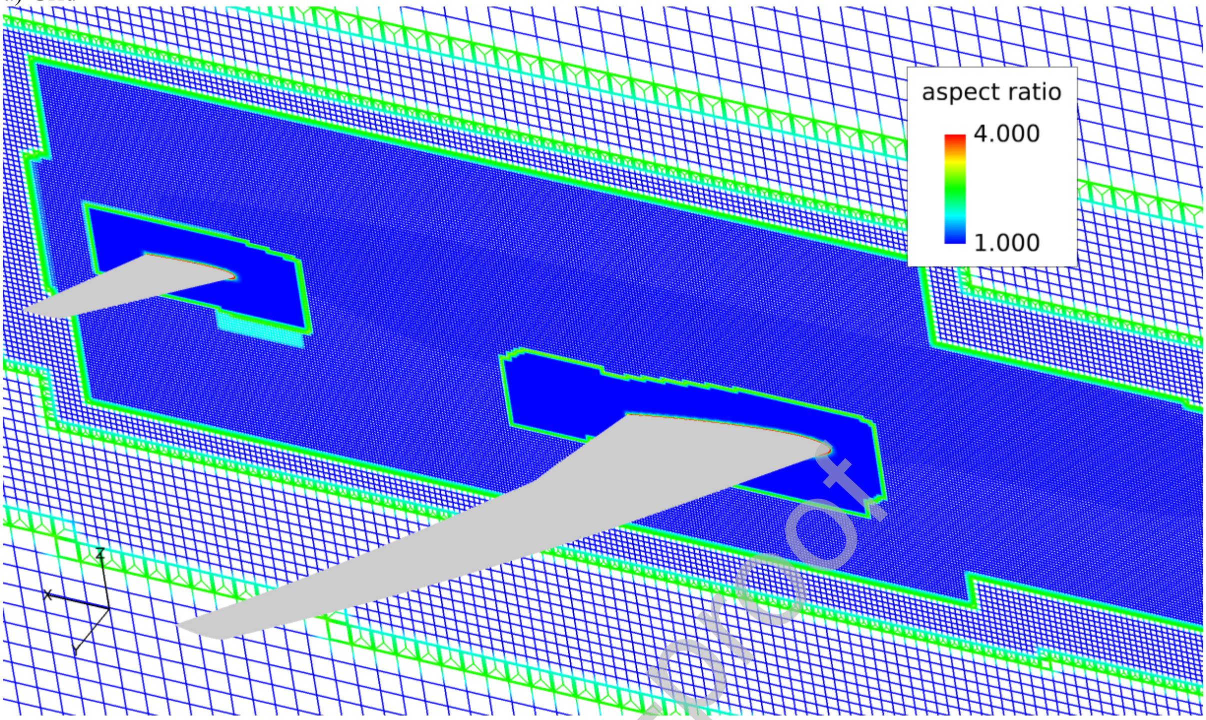

b) Surface Pressure Distribution

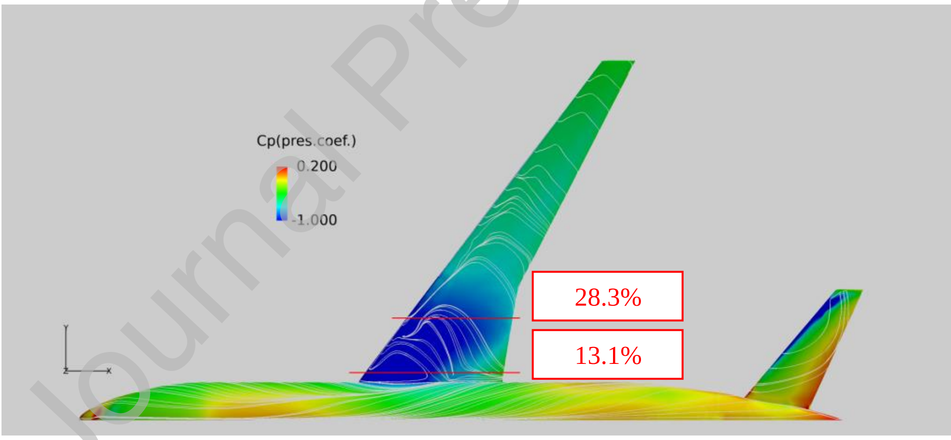

Fig. 11. NASA CRM (a) Computational mesh and (b) Computational solution (surface pressure distribution).

The slope limiter that was employed was Hishida (vL) [47], and the HR-SLAU2 flux function was used unless otherwise stated. The gradient was evaluated by GreenGauss method the turbulence model selected was SA-noft2-R-based DDES, and LU-SGS with a second-order backward difference (five inner iterations, in agreement with [29]) with the local CFL varying from 0.087 in the farfield to 189 near the wall, i.e., $\Delta t \simeq 0.025$ [-]] was adopted for the unsteady computations (The temporal studies are shown in Appendix B; however, the grid-quality studies have not been conducted because the grid-convergence was already reported to be within the range of 3.2

million – 37 million cells in [26]). Then, solutions between 45,000 and 63,000 timesteps were time averaged such that the pressure distribution (Fig. 11b) corresponded to the results from other studies. Nevertheless, the pressure distributions near the wing root varied among different studies, and they significantly deviated from the experimental values [3]. In this study, we focused on these pressure discrepancies, and not the details of the flow unsteadiness. In addition, the surface roughness is not considered as in Ref. [3].

5.1. Effects of C_{DES}

First, we investigate the effects of C_{DES}, which was mentioned above in the first numerical example. The recommended value for C_{DES} is 0.65 [33], as used in several other cases in literature. However, Mohamed et al. [7] used a smaller value, $C_{DES} = 0.51$, along with a reduced-dissipation version of Roe flux (which was later called HR-Roe [25]) and demonstrated its ability to handle isotropic turbulence accurately. Thus, in the present work, the C_{DES} value was varied from 0.65 to 0.51, and even up to 0.10 for DDES.

The computed C_p distributions are compared at $\eta = 13.1\%$ spanwise station, at which the experimental data are known to be hardly captured by computational fluid dynamics (CFD) (Fig. 12). From this figure, it is obvious that lowering the C_{DES} (= extending the LES region) affected the solutions so that they approach the experimental data values. However, it was difficult to determine the validity of the case with $C_{DES} = 0.10$ case (designated as “cdes010”) because it had no other reference data, and it showed slight oscillations over both the upper and lower wing surfaces. This may have resulted from the improper treatment of the prism cells around the body (for the boundary-layers), which were almost entirely covered by the LES regions, as opposed to the case with $C_{DES} = 0.51$ (Fig. 13). Therefore, we will select $C_{DES} = 0.51$ based on the current result and that proposed by Mohamed et al. [7]. In addition, the C_{DES}=1.0 case was conducted, denoted as “cdes100,” leading to higher discrepancies with the experiment, whereas C_{DES}=0.0 stopped the computation at the very beginning.

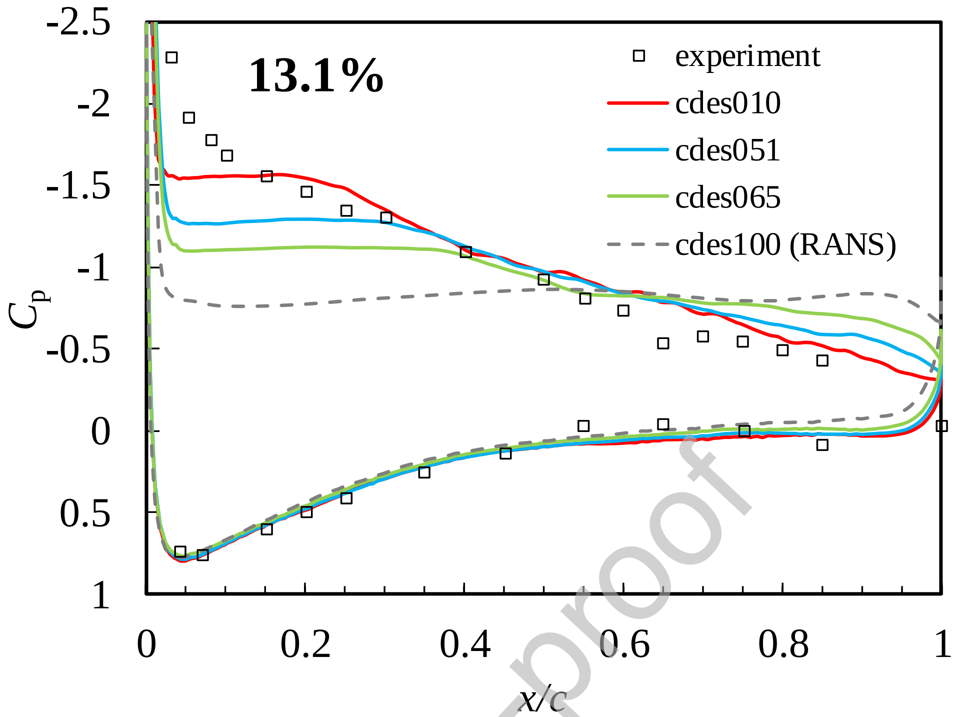

Fig. 12. Effects of C_{DES}: C_p distributions at 13.1% spanwise station [Experimental values were taken from Ref. [3]].

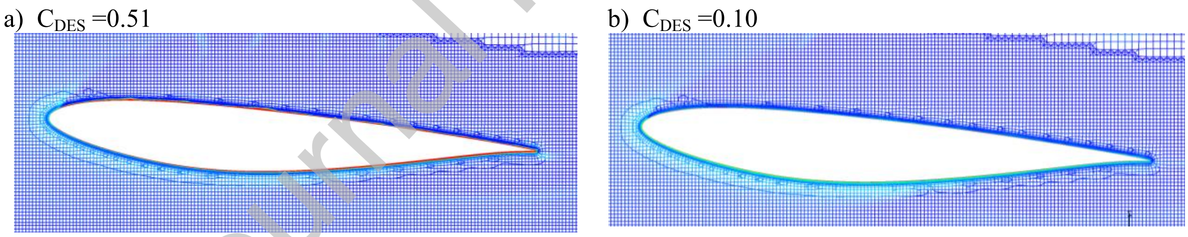

Fig. 13. Computational grid around NASA CRM main wing at η=13.1%, colored with (non-dimensional length scale) = (LES length scale Δ) / (RANS length scale d). 0 (blue) almost corresponds to LES regions, and 1 (red) for RANS regions (the function f_d leads all of the near-wall regions to RANS), (a) C_{DES} =0.51 and (b) C_{DES} =0.10.

5.2. Effects of C_{rot}

The effects of C_{rot} are examined with C_{DES} = 0.51. Now, the C_p distributions at η = 28.3% spanwise location are compared (Fig. 14a) rather than at η = 13.1% at which only slight differences were observed. Moreover, the corresponding velocity vectors around the leading edge are shown in Fig. 14b (C_{rot} = 0.0) and Fig. 14c (C_{rot} = 2.0). The case with C_{rot} = 1.0 was very similar to that with C_{rot} = 2.0, and it was hence omitted in this figure.

From these figures, it is observed that the C_p distributions are affected by C_{rot} around the leading edge, i.e., x/c = 0.05-0.1, although no strange leading-edge separation is clearly seen from either case (Fig. 14b,c). Such a C_{rot}-dependence partially supports the results obtained in the previous example and other works [10-12]. As such, C_{rot} = 2.0 is selected because it appears to have suppressed nonphysical leading-edge separation, as also confirmed in Section 4.1.

a) C_p

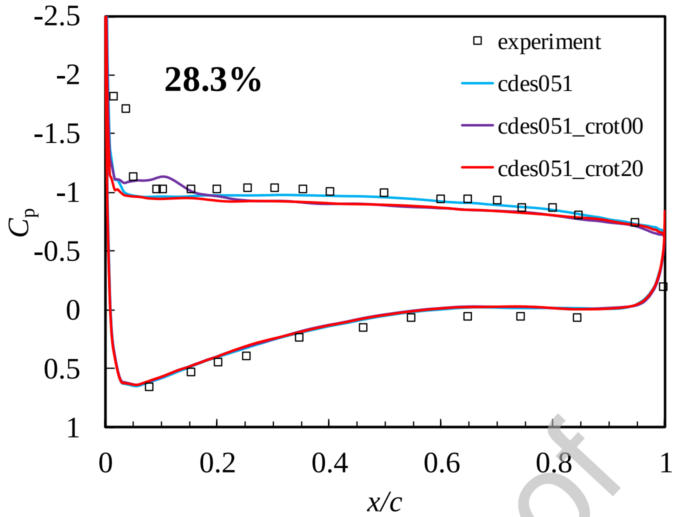

b) C_{rot} =0.0

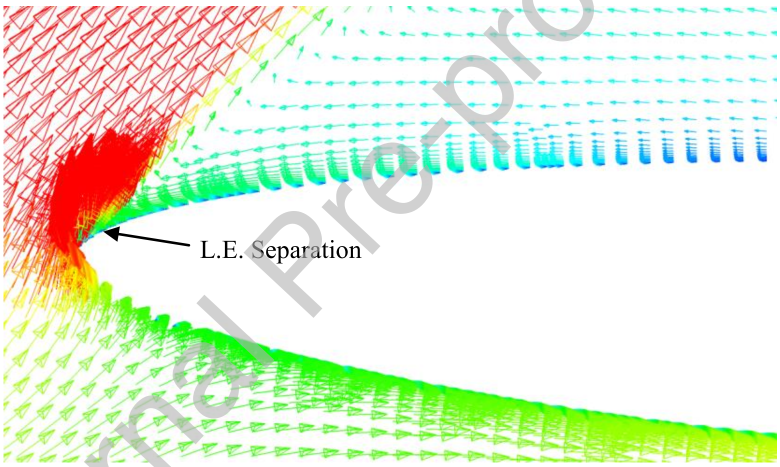

c) C_{rot} =2.0

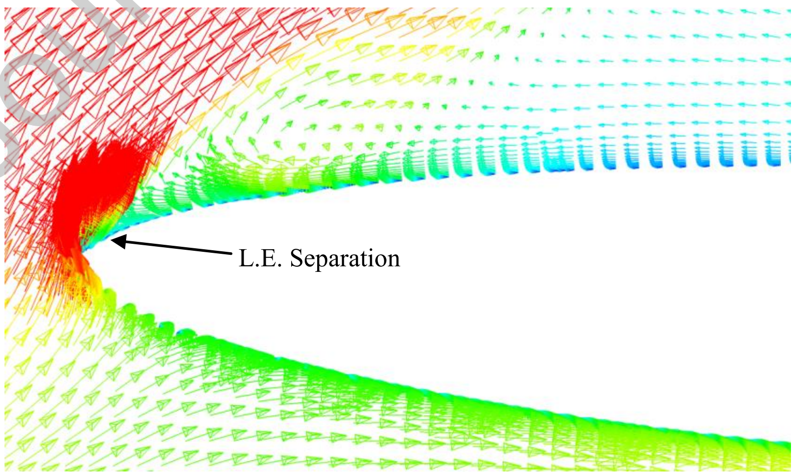

Fig. 14. Effects of C_{rot}: (a) C_p distributions at 28.3% spanwise station, (b) Velocity vectors near the leading-edge (L.E.) colored with Mach number (C_{rot} =1.0), and (c) (C_{rot} =2.0) [Experimental values were taken from Ref. [3]].

5.3. Comparison with conventional approaches

Based on the discussion herein, the following three different methods are compared in Fig. 15:

- "Conventional (DDES)": The conventional DDES with the HR-SLAU2.
- "Conventional, C_{DES} = 0.51, C_{rot} =2.0 (DDES)": The DDES with the proposed modifications (C_{DES} = 0.51, C_{rot} = 2.0) along with HR-SLAU2.
- "Present": The DDES with the proposed modifications (C_{DES} = 0.51, C_{rot} = 2.0) along with HR-SLAU2 and the modified LES/RANS transition (The dirty-cell treatments explained in section 3.4).

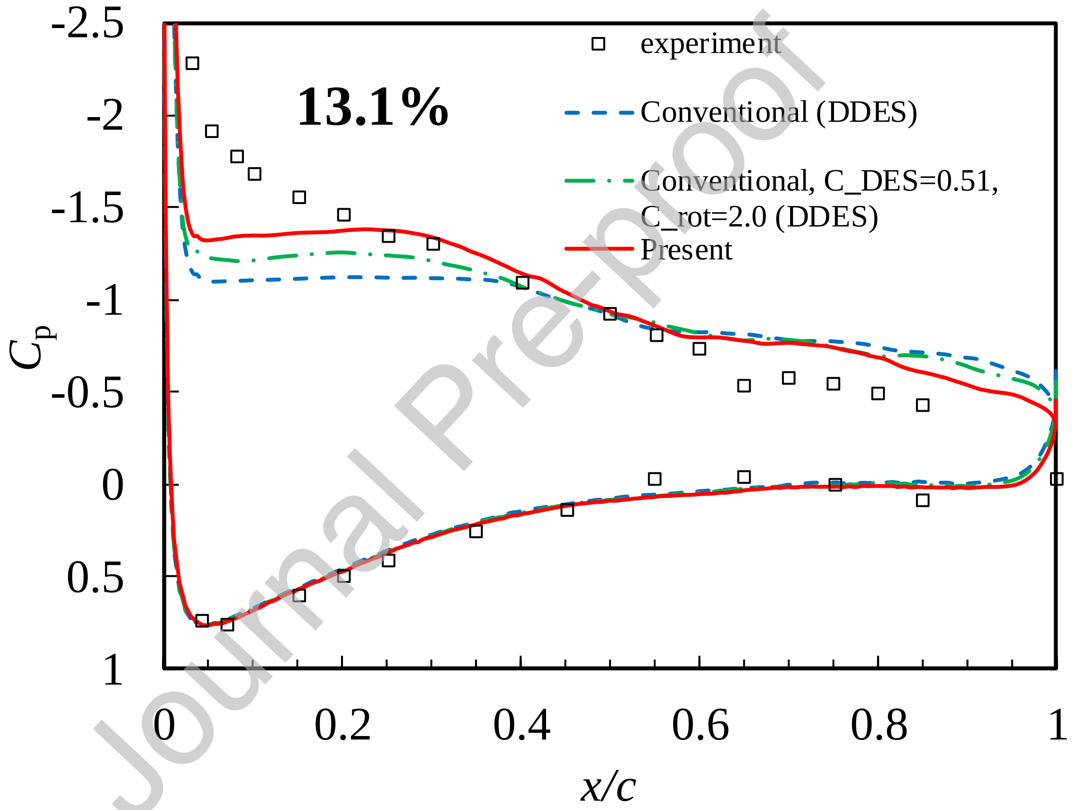

Fig. 15. C_p distributions at 13.1% spanwise station: Comparison with "Conventional DDES" [Experimental values were taken from Ref. [3]].

From this figure, although a perfect agreement with the experiment was not realized, the present modification obviously captured it better than the other solutions did. This was because of the modified treatment for the LES/RANS transition. Furthermore, the HR-SLAU2 with the modified C_{DES} and C_{rot} was closer to the measured data than the original DDES. In the future, we can try to dynamically control C_{DES} and C_{rot} based on these results.

6. Conclusions

In this study, we investigated the leading-edge separation behaviors due to coefficients of SA and SA-based DDES, and proposed simple modifications for unsteady turbulent flow computations, which is represented by a low-speed buffet involving a leading-edge separation. The modified DDES consists of the following for high-resolution computations.

- The SA-R coefficient C_{rot} is re-investigated for a better leading-edge separation prediction in DDES (C_{rot} = 2.0)
- The LES/RANS boundary is calibrated for dissipation control in DDES (LES coefficient C_{DES} = 0.51)
- Dirty-cell (cell aspect ratio *AR* > 4) treatments in 3D unstructured grids for smooth LES/RANS transition

From the SA-RANS results,

- The effects of C_{rot} can be divided into two categories into two: i) fully-developed boundary-layer separation at downstream; and ii) the boundary-layer separation under its development, such as the leading-edge separation.
- In i), C_{rot} = 0.0 showed an excess amount of turbulent viscosity, creating a large but weak vortex, whereas C_{rot} = 1.0 or 2.0 picked up the turbulent viscosity contribution from the pure rotation, leading to an improved better capturing of a vortex.
- In ii), as opposed to i), the larger C_{rot} suppressed the intensity of the separation vortex. However, special care must be taken for C_{rot} = 1.0, whose effects did not appear sufficient enough to clearly distinguish the pure rotation effects from the turbulence.
- The rocket example, where C_{rot} = 2.0, showed the closest pitching moment value to the reference. However, we cannot assume that C_{rot} = 2.0 is the best choice based only on this example. Furthermore, similar results were obtained in our preliminary computations for different flow conditions around different configurations. In addition, at least for DDES, the RANS should play an important role in the leading-edge separation. Therefore, we focused on ii), and we selected the C_{rot} value that can handle the leading-edge separation. In this respect, the case with C_{rot} = 2.0 appears promising.

From the SA-based DDES results, the computational solution on the main wing of NASA CRM has been significantly improved, although it had earlier been in poor agreement with the experimental data. Further improvements are expected if the model coefficients C_{DES} and C_{rot} will be dynamically provided based on the solutions.

Declaration of interests

☒ The authors declare that they have no known competing financial interests or personal relationships that could have appeared to influence the work reported in this paper.

☐The authors declare the following financial interests/personal relationships which may be considered as potential competing interests:

CRediT authorship contribution statement

K. Kitamura: Conceptualization, Methodology, Software, Formal analysis, Writing - Original Draft, Visualization, Project administration, Funding acquisition
Y. Takagi: Validation, Investigation, Data Curation, Visualization
T. Harada: Validation, Investigation, Data Curation, Visualization
Y. Yasumura: Validation, Investigation, Data Curation, Visualization
M. Kanamori: Resources, Writing - Review & Editing, Supervision
A. Hashimoto: Resources, Writing - Review & Editing, Supervision

Acknowledgments

The flow solver used here was FaSTAR, which was developed at JAXA, as well as the mesh generators HexaGrid and MEGG3D. We appreciate the computational assistance provided by JAXA's Supercomputer System (JSS) 2. We thank Suguru Ogawa and Hiroyuki Takimoto, alumni of our group, for conducting a part of computations. We also thank members of our group: Tomohiro Mamashita and Fumiya Tsutsui for helping us with data processing, and Yoshikatsu Furusawa for having fruitful discussions. We would like to thank Editage (www.editage.com) for the English language editing provided. This work was partially supported by JSPS KAKENHI Grant Number JP19K04834.

Appendices

A. SA Model

The SA model, which is a one-equation RANS model, solves the following equations.

$$\frac{D\tilde{\nu}}{Dt} = c_{b1}[1-f_{t2}]\tilde{S}\tilde{\nu} + \frac{1}{\sigma}\left[\nabla\cdot((\nu+\tilde{\nu})\nabla\tilde{\nu}) + c_{b2}(\nabla\tilde{\nu})^2\right] - \left[c_{w1}f_w - \frac{c_{b1}}{\kappa^2}f_{t2}\right]\left[\frac{\tilde{\nu}}{d}\right]^2 \quad \text{(A.1)}$$

$$\nu_t = \tilde{\nu}f_{v1}, \quad f_{v1} = \frac{\chi^3}{\chi^3 + c_{v1}^3}, \quad \chi \equiv \frac{\tilde{\nu}}{\nu} \quad \text{(A.2)}$$

$$\tilde{S} = |\omega| + \frac{\tilde{\nu}}{\kappa^2 d^2} f_{v2}, \quad f_{v2} = 1 - \frac{\chi}{1+\chi f_{v1}} \quad \text{(A.3)}$$

$$\left. \begin{aligned} & f_w = g\left[\frac{1+c_{w3}^6}{g^6 + c_{w3}^6}\right]^{1/6}, \\ & g = r + c_{w2}(r^6 - r), \quad r \equiv \frac{\tilde{\nu}}{\tilde{S}\kappa^2 d^2} \end{aligned} \right\} \quad \text{(A.4)}$$

$$f_{t2} = c_{t3}\exp(-c_{t4}\chi^2) \quad \text{(A.5)}$$

Eq. (A.1) is solved for the working variable $\tilde{\nu}$ defined in Eq. (A.2), where $|\omega|$ is the vorticity magnitude.

$$|\omega| = \sqrt{\left(\frac{\partial v}{\partial x} - \frac{\partial u}{\partial y}\right)^2 + \left(\frac{\partial w}{\partial y} - \frac{\partial v}{\partial z}\right)^2 + \left(\frac{\partial u}{\partial z} - \frac{\partial w}{\partial x}\right)^2} \quad \text{(A.6)}$$

In the SA-R model, this $|\omega|$ is replaced by Eq. (3).

The "*d*" is the wall distance (Fig. 1). The SA-model (and its variants) do not have to search for this *d* along the grid line, and hence, can be readily used on unstructured grids. The coefficients are $\sigma = 2/3$, $c_{b1} = 0.1355$, $c_{b2} = 0.622$, $c_{v1} = 7.1$, $\kappa = 0.41$, $c_{w1} = c_{b1}/\kappa^2 + (1+c_{b2})/\sigma$, $c_{w2} = 0.3$, $c_{w3} = 2$. The original SA model employs $c_{t3} = 1.2$ and $c_{t4} = 0.5$, whereas $c_{t3} = 0.0$ in the SA-noft2 model (and thus $f_{t2} = 0$, and c_{t4} are no longer required) is used in this study. Consequently, the turbulent transition is not triggered by the c_{t3}.

B. Temporal Studies on "5. 3D Low-Speed Buffet Flow Computation"

In order to confirm the validity of the temporal interval and average length, we prepared computed solutions using i) three different values, i.e., $\Delta t \fallingdotseq 0.0125$ [-], 0.025 (adopted) [-], and 0.05 [-], and ii) three different time lengths for averaging, i.e., 45,000–63,000 steps (adopted), 63,000–81,000 steps, and 45,000–81,000 steps. The results are shown in Figs. B1, B2, and B3, respectively, which all demonstrate the validity of the adopted time step size and averaging duration, i.e., smaller time steps or longer time durations resulted in very similar solutions to the default (adopted) ones. In addition, the lift coefficient C_L obtained by $\Delta t \simeq 0.0125$ [-] and 0.025 (adopted) [-] are fluctuating between 1.00 – 1.10, which is consistent with results from previous studies [3].

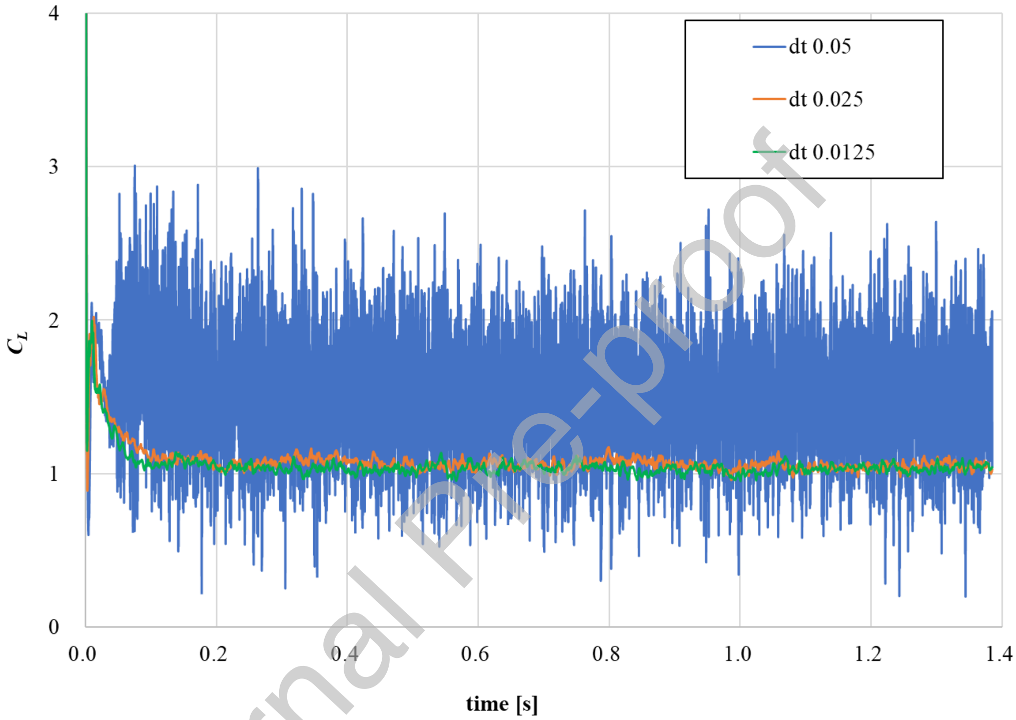

Fig. B1. C_L histories using different time intervals.

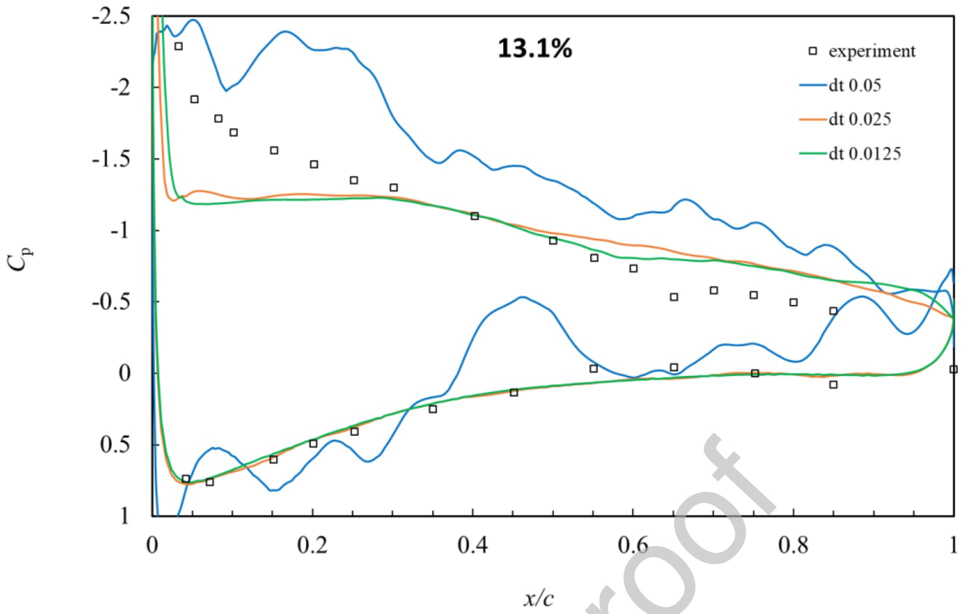

x/c

Fig. B3. C_p distributions at 13.1% spanwise station using different time average durations.

References

1) Deck, S.: Numerical Simulation of Transonic Buffet over a Supercritical Airfoil, *AIAA J.*, Vol. 43, No. 7, 2005, pp.1556–1566.

2) Sartor, F., and Timme, S.: Delayed Detached–Eddy Simulation of Shock Buffet on Half Wing–Body Configuration, *AIAA J.*, Vol. 55, No. 4, 2017, pp.1230-1240.

3) Waldmann, A., Gansel, P.P., Lutz, T., and Krämer, E., "Unsteady Wake Flow Analysis of an Aircraft under low-speed Stall Conditions using DES and PIV", AIAA 2015-1096, 2015.

4) Dandois, J., Mary I., and Brion, V.: Large-eddy simulation of laminar transonic buffet, *J. Fluid Mech.*, Vol. 850, 2018, pp.156-178.

5) Kouchi, T., Yamaguchi, S., Koike, S., Nakajima, T., Sato, M., Kanda, H. & Yanase, S., Wavelet analysis of transonic buffet on a two-dimensional airfoil with vortex generators, *Exp. Fluids*, Vol. 57, 2016, Article Number 166. https://doi.org/10.1007/s00348-016-2261-2

6) Spalart, P. R., Deck, S., Shur, M. L., Squires, K. D., Strelets, M. Kh., and Travin, A.: A New Version of Detached-Eddy

Simulation, Resistant to Ambiguous Grid Densities, *Theor. and Comput. Fluid Dynamics*, Vol. 20, 2006, pp. 181-195.

7) Mohamed, K., Nadarajah, S., and Paraschivoiu, M.: Detached-Eddy Simulation of a Wing Tip Vortex at Dynamic Stall Conditions, *Journal of Aircraft*, Vol. 46, No. 4, 2009, pp. 1302–1313.

8) Spalart, P., and Allmaras, S., "A One-Equation Turbulence Model for Aerodynamic Flows," AIAA 1992-439, 1992.

9) Rumsey, C. L.: Apparent Transition Behavior of Widely-used Turbulence Models, *Int. J. Heat and Fluid Flow*, Vol. 28, 2007, pp. 1460–1471.

10) Dacles-Mariani, J., Kwak, D., and Zilliac, G.: On Numerical Errors and Turbulence Modeling in Tip Vortex Flow Prediction, *Int. J. Numer. Meth. Fluids*, Vol. 30, 1999, pp. 65-82.

11) Dacles-Mariani, J., Zilliac, G.G., Chow, J. and Bradshaw, P.: Numerical/Experimental Study of a Wingtip Vortex in the Near Field, *AIAA J.*, Vol. 33, No. 9, 1995, pp. 1561–1568.

12) Lei, Z.: Effect of RANS Turbulence Models on Computation of Vortical Flow over Wing-Body Configuration, *Trans. Japan Soc. Aero. Space Sci.*, Vol. 48, No. 161, 2005, pp. 152-160.

13) NASA Langley Research Center, "Turbulence Modeling Resource" https://turbmodels.larc.nasa.gov/spalart.html (Accessed on May-03-2019)

14) Kwak, D., Ohira, K. and Rudnik, R.: Reynolds Number Effect on Vortex Dominant Flow of the SST Configurations, APISAT2014, Session 1-7-3, 2014.

15) Spalart P.R., Jou W.-H., Strelets M., and Allmaras S.R.: Comments on the feasibility of LES for wings, and on a hybrid RANS/LES approach. In Advances in DNS/LES, ed. C Liu, Z Liu, 1997, pp. 137–47. Columbus, OH: Greyden Press

16) Shur ML, Spalart PR, Strelets MKh, Travin A.: A hybrid RANS-LES model with delayed DES and wall-modeled LES capabilities, *Int. J. Heat Fluid Flow*, Vol. 29, 2008, pp. 1638–1649. doi:10.1016/j.ijheatfluidflow.2008.07.001

17) Tucker, P.G.: Unsteady Computational Fluid Dynamics in Aeronautics (Fluid Mechanics and Its Applications), Springer, Berlin Heidelberg, 2014. ISBN-13: 978-9402405743

18) Spalart, P.R., Detached-Eddy Simulation, *Annual Review of Fluid Mechanics*, Vol. 41, pp.181-202, 2009. 10.1146/annurev.fluid.010908.165130

19) Vatsa, V.N., Lockard, D.P., and Spalart, P.R.: Grid Sensitivity of SA-Based Delayed-Detached-Eddy-Simulation Model for Blunt-Body Flows, *AIAA Journal*, Vol. 55, No. 8, 2017, pp.2842-2847. https://doi.org/10.2514/1.J055685

20) Molina, E., Zhou, B.Y., Alonso, J.J., Righi M., and Silva, R.G.: Flow and Noise Predictions Around Tandem Cylinders using DDES approach with SU2, AIAA 2019-0326, AIAA Scitech 2019 Forum, 7-11 January 2019, San Diego, California.

21) Kitamura, K. and Hashimoto, A.: Reduced dissipation AUSM-family fluxes: HR-SLAU2 and HR-AUSM^{+}-up for high resolution unsteady flow simulations, *Computers and Fluids*, Vol. 126, 2016, pp. 41–57.

22) Kitamura, K. and Shima, E.: Towards shock-stable and accurate hypersonic heating computations: A new pressure flux for

AUSM-family schemes, *J. Comput. Phys.*, Vol.245, 2013, pp.62-83.

23) Thornber, B.J.R. and Drikakis, D.: Numerical dissipation of upwind schemes in low Mach flow, *International Journal for Numerical Methods in Fluids*, Vol. 56, No. 8, 2008, pp.1535-1541.

24) Roe, P.L.: Characteristic-based schemes for the Euler equations, *Ann. Rev. Fluid Mech.*, Vol. 18, 1986, pp. 337–365.

25) Winkler, C.M., Dorgany, A.J. and Mani, M.: A reduced dissipation approach for unsteady flows on unstructured grids. AIAA 2012-0570, 2012.

26) Hashimoto, A., Murakami, K., Aoyama, T., Yamamoto, K., Murayama, M. and Lahur, P. R.: Drag Prediction on NASA Common Research Model Using Automatic Hexahedra Grid-Generation Method, *J. Aircraft*, Vol.51, 2014, pp. 1172-1182.

27) Ito, Y., and Nakahashi, K.: Direct Surface Triangulation Using Stereolithography Data, *AIAA J.*, Vol. 40, 2002, pp. 490-496.

28) Hashimoto, A., Murakami, K., Aoyama, T., Hishida, M., Sakashita, M., and Lahur, P.: Development of Fast Unstructured-Grid Flow Solver FaSTAR, *Journal of Japan Society for Aeronautical and Space Sciences*, Vol. 63, 2015, pp. 96-105 (in Japanese).

29) Kitamura, K., Aogaki, T., Inatomi, A., Fukumoto, K., Takahama, T., and Hashimoto, A.: Post Limiters and Simple Dirty-Cell Detection for Three-Dimensional, Unstructured, (Unlimited) Aerodynamic Simulations, *AIAA J.*, Vol. 56, No. 8, 2018, pp. 3192-3204. doi:10.2514/1.J056683

30) Kanamori, M., Takahashi, T., Makino, Y., Naka, Y., and Ishikawa, H.: Comparison of Simulated Sonic Boom in Stratified Atmosphere with Flight Test Measurements, *AIAA J.*, Vol. 56, No. 7, 2018, pp. 2743-2755.

31) Sutherland, W., LII.: The viscosity of gases and molecular force, *Philosophical Magazine Series*, Vol.5, No.36, 223, 1893, pp.507-531, DOI: 10.1080/14786449308620508

32) Baldwin, B. S., and Barth, T. J.: A One-Equation Transport Model for High Reynolds Number Wall-Bounded Flows," NASA TM 102847, Aug. 1990.

33) Strelets, M.: Detached Eddy Simulation of Massively Separated Flows, AlAA 2001-0879, 39th Aerospace Sciences Meeting and Exhibit, Jan. 08-11, 2001, Reno, NV.

34) Panaras, A. and Drikakis, D.: High-speed unsteady flows around spiked-blunt bodies, *Journal of Fluid Mechanics*, Vol. 632, 2009, pp.69-96.

35) Aogaki, T., Kitamura, K., and Nonaka, S.: High Angle-of-Attack Pitching Moment Characteristics of Slender-Bodied Reusable Rocket, *Journal of Spacecraft and Rockets*, Vol. 55, No. 6, 2018, pp.1476-1489. doi:10.2514/1.A34211

36) Takagi, Y., Aogaki, T., Kitamura, K., and Nonaka, S.: Numerical Study on Aerodynamic Characteristics of Slender-bodied Reusable Rockets Using Fins and Vortex Flaps at Very High Angles of Attack, *Trans. JSASS, Aerospace Tech. Japan*, Vol. 18, No. 4, pp. 149-158, 2020.

37) Weiss, J.M. and Smith, W.A.: Preconditioning Applied to Variable and Constant Density Flows, *AIAA J.*, Vol. 33, 1995, pp.

2050-2057.

38) Venkatakrishnan, V.: Convergence to Steady State Solutions of the Euler Equations on Unstructured Grids with Limiters, *J. Comput. Phys.*, Vol.118, 1995, pp.120-130.

39) Burg, C. O. E.: Higher Order Variable Extrapolation for Unstructured Finite Volume RANS Flow Solvers, 17th AIAA Computational Fluid Dynamics Conference, Toronto, Ontario, Canada, AIAA 2005-4999, 2005.

40) Harada, T., Kawauchi, K., Kitamura, K., and Nonaka, S.: Side Force Characteristics of Supersonic Flight Vehicle Equipped with Asymmetric Protuberance, AIAA 2019-0299, AIAA SciTech Forum 2019, San Diego, CA, Jan. 2019.

41) Kawauchi, K., Harada, T., Kitamura, K., and Nonaka, S.: Experimental and Numerical Investigations of Slender Body Side Force with Asymmetric Protuberances, *Journal of Spacecraft and Rockets*, Vol. 56, No. 5, 2019, pp. 1346–1357. doi:10.2514/1.A34439

42) Mavriplis, D. J., "Revisiting the Least-Squares Procedure for Gradient Reconstruction on Unstructured Meshes," AIAA 2003-3986, 2003.

43) Roe, P.L.: Characteristic-based schemes for the Euler equations, *Ann. Rev. Fluid Mech.*, Vol. 18, 1986, pp.337–365.

44) Van Leer, B.: Towards the Ultimate Conservative Difference Scheme. V. A Second-Order Sequel to Godunov's Method, *J. Comput. Phys.*, Vol. 32, 1979, pp.101-136.

45) Shima, E. and Kitamura, K.: Parameter Free, Simple, Low-dissipation AUSM-family Scheme for All Speeds, *AIAA J.*, Vol.49, 2011, pp.1693-1709.

46) Jameson, A. and Turkel, E.: Implicit Schemes and LU Decompositions, *Math. of Comput.*, Vol. 37, 1981, pp.385-397.

47) Hishida, M., Hashimoto, A., Murakami, K., and Aoyama, T., "A New Slope Limiter for Fast Unstructured CFD Solver FaSTAR," *JAXA-SP-10-012*, JAXA, Tokyo, 2011, pp. 85–90 (in Japanese).